

Electrodeposited Magnetic Nanoporous Membrane (MNM) with a Multi-Edge Superparamagnetic Heterogeneous Wedge Junction for High-Yield and High-Throughput Immunocapture of Specific Extracellular Vesicles and Lipoproteins

Chenguang Zhang

University of Notre Dame <https://orcid.org/0000-0001-5124-875X>

Xiaoye Huo

University of Notre Dame

Yini Zhu

University of Notre Dame

James Higginbotham

Vanderbilt University Medical Center

Xin Lu

Notre Dame <https://orcid.org/0000-0002-0284-6478>

Jeffrey Franklin

Vanderbilt University Medical Center

Kasey C. Vickers

Vanderbilt University Medical Center

Robert Coffey

Vanderbilt University Medical Center

Satyajyoti Senapati

University of Notre Dame <https://orcid.org/0000-0001-7999-1561>

Ceming Wang

University of Notre Dame <https://orcid.org/0000-0002-1328-6410>

Hsueh-Chia Chang (✉ hchang@nd.edu)

University of Notre Dame <https://orcid.org/0000-0003-2147-9260>

Article

Keywords: Extracellular Vesicle, Superparamagnetic, Immunocapture

Posted Date: March 23rd, 2022

DOI: <https://doi.org/10.21203/rs.3.rs-1448269/v1>

License:  This work is licensed under a Creative Commons Attribution 4.0 International License.

[Read Full License](#)

1 **Electrodeposited Magnetic Nanoporous Membrane (MNM) with a**
2 **Multi-Edge Superparamagnetic Heterogeneous Wedge Junction for**
3 **High-Yield and High-Throughput Immunocapture of Specific**
4 **Extracellular Vesicles and Lipoproteins**

5 Chenguang Zhang^{1,#}, Xiaoye Huo^{1,#}, Yini Zhu², James N. Higginbotham³, Xin Lu², Jeffrey L. Frank-
6 lin^{3,4}, Kasey C. Vickers³, Robert J. Coffey^{3,4}, Satyajyoti Senapati¹, Ceming Wang^{5,*}, Hsueh-Chia
7 Chang^{1,*}

8 ¹ Department of Chemical and Biomolecular Engineering, University of Notre Dame, Notre Dame, IN 46556,
9 USA.

10 ² Department of Biology, University of Notre Dame, Notre Dame, IN 46556, USA.

11 ³ Department of Medicine, Vanderbilt University Medical Center, Nashville, TN 37232, USA.

12 ⁴ Department of Cell and Developmental Biology, Vanderbilt University School of Medicine, Nashville, TN
13 37232, USA.

14 ⁵ Aopia Biosciences, 31351 Medallion Dr, Hayward, CA 94544, USA.

15 # These authors contributed equally: Chenguang Zhang, Xiaoye Huo.

16 corresponding author email: cwang9@nd.edu, hchang@nd.edu

17 **Abstract.** Superparamagnetic nanobeads offer several advantages over microbeads for immunocapture of specific
18 molecular nanocarriers (extracellular vesicles, lipoproteins, and viruses) in a bioassay: high-yield capture, reduction
19 in incubation time and higher capture capacity. However, nanobeads are difficult to “pull down” because their su-
20 perparamagnetic feature requires high nanoscale magnetic field gradients in addition to high magnetic fields. Here,
21 electroplated track-etched membrane is shown to produce a unique superparamagnetic nanowedge ring with multiple
22 edges around each nanopore. With a uniform external magnetic field, the induced monopole and dipole of this nan-
23 owedge junction combine to produce a 10x higher nanobead trapping force. A dense nanobead suspension can be
24 filtered through the magnetic nanoporous membrane (MNM) at a high-throughput with 99% bead capture rate. The
25 capture yield of specific nanocarriers in heterogeneous media (filtered plasma and conditioned cell media) by nano-
26 beads/MNM exceeds 80%. Quantification of RNA cargo in captured extracellular vesicles demonstrate 60x increase
27 in capture rate of a specific microRNA relative to magnetic bead columns. Reproducibility, low loss, and concen-
28 tration-independent capture rates are also demonstrated. This new MNM material hence significantly expands the

29 application of nanobead immunocapture to heterogeneous physiological samples, such as blood and saliva, whose
30 molecular analytes are cargoes of nanocarriers.

31 **Keywords:** Extracellular Vesicle, Superparamagnetic, Immunocapture

32

33 **1 Introduction**

34 Extracellular vesicles (EVs) and lipoproteins are biological nanoparticles that can be found in various
35 biological fluids¹⁻³. Their recently discovered function of delivering molecular cargo between cells has
36 catalyzed considerable research activity in many fields^{4,5}. These biological nanocarriers may be critical
37 mediators of intercellular communication^{6,7}. Thus, specific EVs, lipoproteins, and their molecular cargoes
38 are also potential disease biomarkers⁸⁻¹⁰. However, these biomarkers are often not unique to diseased
39 cells but are simply overexpressed. Consequently, precise quantification is required. Due to their size
40 and heterogeneity, high-yield isolation of specific EVs and lipoproteins remains challenging and may
41 introduce significant bias in the biomarker assay¹¹⁻¹⁵. EVs and lipoproteins also tend to degrade, aggre-
42 gate, or adsorb in many devices^{16,17}. Thus, immediate and short-contact isolation is preferred over flow
43 cytometry and chromatograph separation, whose pre-treatment/separation processes are long and com-
44 plex. An effective, rapid, and accessible isolation method is hence a prerequisite for any clinical appli-
45 cation involving EVs and lipoproteins. Advances in high-yield capture technologies are beneficial across
46 many biomedical spaces, including for the detection of pathogenic viruses or bacteria.

47

48 The most specific EV and lipoprotein isolation method is immuno-capture¹⁸⁻²⁰; however, traditional
49 immuno-capture technologies, like immuno-precipitation (IP) and immuno-affinity chromatography,
50 have low-yield issues due to probe saturation and analyte loss. If the nanocarriers are fluorescently la-
51 belled, those captured by magnetic microbeads can be sorted and quantified by flow cytometry. However,
52 the labeling and isolation process is time-consuming and may require more than one day to achieve
53 optimal yield, resulting in significant nanocarrier loss. Their throughputs are also limited by the long
54 incubation time (8-48 hrs) because of the low mobility of microbeads for the transport-limited docking

55 reaction. A solution to this yield and incubation time issues is to use nanomagnetic beads. Their large
56 surface area per volume provides more binding sites. Their smaller size leads to higher diffusivity and a
57 shorter incubation time (approximately 30min). The beads can also diffuse through a heterogeneous
58 physiological sample to capture specific nanoparticle targets that have reduced mobility due to complex-
59 ification or aggregation. Their large surface area per volume provides more binding probes, by a factor
60 equal to the ratio of the microbead/nanobead radii (~ 100) for the same bead weight concentration. This
61 significant increase in the probe number can lead to complete depletion of all the target nanocarriers,
62 particularly if the antibody probes have high affinity, thus providing orders of magnitude higher nanocar-
63 rier binding yield. Their smaller size leads to higher diffusivity and a shorter incubation time (approx-
64 imately 30 min). The beads can also diffuse through a heterogeneous physiological sample to capture
65 specific nanocarrier targets that have reduced mobility due to complexification or aggregation.

66

67 However, due to their superparamagnetic nature, it is difficult to trap nanobeads and their captured
68 nanocarriers after bulk immuno-capture. The magnetic force on the superparamagnetic beads is propor-
69 tional to the gradient of field squared (twice the product of the field and field gradient), whereas the force
70 on a magnetic microbead is proportional to the local field. For the commonly used magnetic microbead
71 traps, the field gradient is confined to less than one radius of the microbead, and hence, can only trap
72 nanobeads within a small area around the microbead. Therefore, a long column of densely packed beads
73 is required for high-yield capture. For example, commercial microbeads columns (μ Column, Milyteni
74 Biotech) for nanobead capture only trap 20-30% of the nanobeads²¹. Repeated ($>4x$) trapping is neces-
75 sary to produce $> 90\%$ yield. A magnetic film can produce a higher field penetration length than a mag-
76 netic bead due to its non-focusing (non-radial) geometry. Recently, Issadore and colleagues developed a
77 magnetic layer-coated nanoporous membrane with improved capture yield, both multiple layers of mem-
78 branes are still required for efficient bead capture²². Although the field is long-range, the field gradient
79 is not for a planar magnetic film, except at corners. In our earlier work on electric fields at microchan-
80 nels²³ and nanopores²⁴, we showed that a singular electric field with high gradient occurs in the high
81 permittivity (water) side of a wedge corner of a channel or a pore if the wedge angle α of the higher
82 permittivity phase exceeds π . This wedge singular field decays radially from the wedge tip with a power
83 law scaling of $-(\pi/\alpha) - 1$ and hence also has a high field gradient. The radial decay exponent is bound
84 between -2 of a sphere and -3/2 of an infinitely long cylinder. This singular wedge mode is antisymmetric

85 around the wedge and introduces a dipole in the high permittivity phase. There is a more well-known
 86 “lightning rod” wedge singularity in near-field plasmonics^{25–27} that is symmetric around the wedge, with
 87 the singular field occurring on the low permittivity side. It occurs when the high-permittivity side has a
 88 wedge angle that is less than π . It introduces a monopole on the low-permittivity side of the wedge.
 89 Herein, we extend this concept to magnetic fields to achieve high-yield capture of superparamagnetic
 90 beads with high-throughput. We designed a multi-edge superparamagnetic NiFe nanowedge with hetero-
 91 geneous junction, whose edges sustain both a magnetic monopole and dipole around each nanopore of
 92 a polymer nanoporous membrane. This approach will significantly increase the capture yield of one
 93 membrane to 99% at a throughput of 5mL/hr for a single magnetic nanoporous membrane (MNM).

94

95 Compared to the smooth pore edge formed during sputtering, edges on the electroplated membrane
 96 are sharper to approach the wedge geometry. Therefore, electroplating was used instead of sputtering for
 97 Ni₈₀Fe₂₀ layer deposition. Moreover, because of the high field at the Au film junction during electroplat-
 98 ing, the NiFe film wraps around the gold layer sputtered inside the pore to form the desired edge geom-
 99 etry for a dipole. The uncaptured EVs can go through the straight pores and be collected in the flow-
 100 through. We proved MNM’s efficiency and specificity using high-density lipoproteins (HDL) as a model,
 101 and observed >80% of HDL is recovered using the method, nearly doubling the recovery rate for com-
 102 mercial kits. We also demonstrated that MNM has a high and consistent yield, and hence, can provide
 103 the necessary statistics for quantifying biomarkers carried by EVs and lipoproteins in heterogeneous
 104 physiological fluids.

105

106 2 Results

107 2.1 Theory and Simulation of Heterogeneous Superparamagnetic Nano-Junction

108 Because the magnetic moment of a superparamagnetic nanobead is induced by the external field, the
 109 force on it is described by:

$$110 \quad \vec{F}_M = \frac{\chi_{eff} V \mu}{2\mu_0} \nabla |\vec{B}|^2 \quad (1)$$

111 Where χ_{eff} is the effective magnetic susceptibility of the beads, V is the bead volume, μ and μ_0 are the
 112 vacuum and material magnetic permittivity, and \vec{B} is the magnetic field. The magnetic force increases as

113 the gradient of field squared or twice the field multiplied by the field gradient. Thus, a high magnetic
114 field gradient is the key to achieving high bead recovery. The geometric enhancement of electromagnetic
115 field has been applied to a variety of engineering designs, from large-scale antenna^{28,29} to nanostruc-
116 tures^{30,31}. Previously, we used the singular electric field at the edge of microchannels²³ and nanopores²⁴
117 to trap colloids and translocating molecules by dielectrophoresis. As shown in Figure 1a and c, the edge
118 of the nanopore on the sputtered membrane is smooth. The NiFe layer only covered the top of Au layer
119 due to the anisotropic nature of sputtering. A sharper edge appeared in the electroplated membrane be-
120 cause of electric field focusing during plating (Figure 1b and d). The NiFe film also grew inside the pore
121 to form the wedge heterogeneous junction, since unlike sputtering, electroplating also occurs on the side
122 of the 80nm gold film. Under uniform external magnetization at 0.4 Tesla, a maximum field of 0.62 Tesla
123 and a maximum gradient of flux density square at $2.3 \times 10^5 \text{ T}^2/\text{cm}$ develops in the water phase (Figure
124 1h), compared to 0.48 Tesla and $2.2 \times 10^4 \text{ T}^2/\text{cm}$ for the sputtered NiFe film without the wedge ring, which
125 represents a 10-fold increase in the force field of (1).

126

127 The high field enhancement originates from a water phase monopole at the upper edge of the NiFe
128 film, where the wedge angle on the high permeability superparamagnetic NiFe phase is approximately
129 $\pi/2$ and a dipole in the NiFe phase at the outer edge at the base of the wedge junction, where the wedge
130 angle on the NiFe side is approximately $3\pi/2$. There is an additional amplification of the dipole field
131 as it enters into the water phase with a magnetic permeability that is 40 times lower. In the sputtered
132 membrane, we only have a weak upper monopole due to the smooth edge (Figure 1g). This combination
133 of the dipole and monopole field at the sharp edges of the electroplated 100nm NiFe film is responsible
134 for the 10x increase in the nanobead trapping force, and we expect to observe a similar increase in capture
135 yield for superparamagnetic nanaobeads.

136

137 2.2 High-Efficiency Capture of Superparamagnetic beads by MNM

138 To test the capture efficiency of the MNM with the multi-edge superparamagnetic wedge around each
139 nanopore, we designed a housing apparatus for MNM immuno-capture applications, and is described in
140 the supporting information. Round membranes with 2cm diameter were tested during the experiments.
141 Briefly, 1mL of 10× diluted 30 nm nanobeads from Exosome Isolation Kit Pan (mouse, Miltenyi Biotec)

142 were passed through the electroplated 450nm (PET pore size) nanoporous membrane at 1mL/hr. Figure
143 2b shows the bead solution before and after magnetic capturing on the membrane; the brownish bead
144 color disappears entirely in the flow-through solution, indicative of high bead capture efficiency. Nano-
145 beads convected by streamlines close to the surface are trapped by the monopole near the top edge of the
146 NiFe film, as shown in Figure 2a. The remaining beads are convected into the pore center and are trapped
147 by the high dipole magnetic force within the pore (Figure 2c).

148

149 The pore size shrinks from 450nm to about 350nm after electroplating, which is still larger than the
150 typical small EV (sEV) size of 30-200 nm, allowing non-target EVs without nanobeads to pass through.
151 A quantitative study of bead capturing efficiency was conducted by comparing the bead concentration
152 measured by nanoparticle tracking analysis (NTA) before and after capturing (see Figure 2e). At
153 1mL/hr, >99% of the beads were captured. The bead capture efficiency did not diminish even at a flow
154 rate of 5mL/hr. This throughput is high enough for most extracellular vesicle immuno-capture applica-
155 tions. Furthermore, only 13% of the beads were lost when the flow rate was increased to 10mL/hr. For
156 membranes with 1 μ m pore size, the bead capture efficiency was still >80% at 1mL/hr. In stark contrast,
157 only 22% of beads were captured by the sputtered 450nm membrane (Figure 2e). For larger vesicles
158 above 300nm, electroplated MNM with 1 μ m pore size can be used at a lower flow rate or with a higher
159 external magnetic field.

160

161 **2.3 Isolation of High-Density Lipoprotein (HDL)**

162 Based on the effectiveness of the MNM to capture EVs, we sought to investigate the capacity of this
163 method to capture lipoproteins, namely HDLs. HDLs are highly-abundant in plasma and other biofluids
164 and provide a good model to trace based on standard cholesterol assays that can be used to quantify them.
165 Apolipoprotein A-I (apoA-I) is the main structure-function protein on the surface of HDL particles.
166 ApoA-I is primarily associated with HDL and accounts for approximately 70% of total HDL protein
167 content by mass. HDL samples were isolated from human plasma by density-gradient ultracentrifugation
168 (DGUC) and total protein levels were quantified by colorimetric assays³². For capture, 2 μ g anti-ApoA-
169 I (Abcam, ab52945, rabbit monoclonal to ApoA1) antibodies were mixed with 100 μ L of 100 μ g/mL HDL
170 sample, incubated for 30min, and treated with 100 μ L anti-rabbit IgG nanobeads (30nm, Milyteni

171 Biotech) for 1 hr. After the HDL were immuno-captured by the magnetic nanobeads, the solution was
 172 diluted to 500 μ L with 1 \times PBS and passed through the 450nm electroplated MNM membrane, followed
 173 by flushing with 1mL 1 \times PBS to bring all beads onto the membrane surface and to remove the residual
 174 HDL solution in the chamber. The flow-through was collected for each sample. The concentration of
 175 cholesterol was measured to calculate the total amount of cholesterol in both the original sample and
 176 flow-through (Figure 3b). The cholesterol capture rate can be calculated as:

$$177 \quad \text{Cholesterol Captured \%} = \frac{\text{Cholesterol}_{\text{original}} - \text{Cholesterol}_{\text{flow-through}}}{\text{Cholesterol}_{\text{original}}} \times 100\% \quad (2)$$

178 Remarkably, >80% of HDL were recovered using this approach. To confirm the specificity of the im-
 179 muno-capture and non-specific adsorption in our device, two negative controls were tested. If no anti-
 180 bodies were functionalized onto the nanobeads in the experiments, < 10% of HDL were lost in the device,
 181 which was due to non-specific adsorption and experimental error. When antibodies against apolipopro-
 182 tein B (ApoB), the structural protein for low-density lipoproteins (LDL), was used instead of anti-ApoA-
 183 I, the loss increased to 14%. The additional 4% loss may come from non-specific capture of HDL by
 184 anti-ApoB. In both negative controls, the nonspecific capture rate of < 15% is significantly lower than
 185 the specific capture rate of 80%. We benchmarked our method to a commercial immuno-capture kit using
 186 their standard protocol (see supporting information). As shown in Figure 3c, for nanobeads, only 20%
 187 HDL were captured by the μ Column (Milyteni Biotech) because of the low bead capture efficiency of
 188 the packed column. Furthermore, for microbeads like DynabeadsTM, even after 16 hrs of incubation,
 189 which is much longer than the standard protocol, the HDL capture efficiency does not exceed 50%. For
 190 the same incubation time of 1 hr as the nanobeads, only 25% HDL was recovered (Figure S4), margin-
 191 ally > 15% non-specific capture rate.

192

193 To further demonstrate the advantage of the MNM immunocapturing method, miRNA extraction and
 194 qRT-PCR quantification of miR-21 were performed on HDL captured by both MNM and DynabeadsTM.
 195 Figure 3d shows a Ct difference of more than 6 between the two immuno-capture methods, which sug-
 196 gests the miRNA expression result of DynabeadsTM 64-fold lower than that of MNM (delta-delta Ct
 197 method). The long incubation time required by microbeads causes sample degradation and miRNA deg-
 198 radation and adsorption, which leads to significant bias in miRNA quantification. In contrast, a high
 199 concentration of miR-21 was preserved in the fast MNM immunocapture.

200

201 **2.4 Purification of EVs in Filtered Plasma**

202 In this demonstration, 100 μ L healthy human plasma was first diluted and processed by tangential flow
203 filtration with 30nm asymmetric nanoporous membranes³³ to remove most of the HDL and other lipo-
204 proteins. As shown in Figure 4b, there was still 17% cholesterol left from mostly LDL and VLDL after
205 filtration. A small amount of HDL could also be present in the filtered sample due to the dominated
206 amount of the HDL in the original plasma. Therefore, we mixed the filtered sample with 2 μ g anti-ApoA-
207 I and 2 μ g anti-ApoB antibodies and incubated for 30min. After adding 200 μ L anti-rabbit IgG mi-
208 croBeads (30nm, Milyteni Biotech) and incubating for 1 hr, the mixture was passed through the MNM.
209 The collected flow-through was the purified EV sample, which contained 85% of the original EV, but
210 only 5% of the original cholesterol. The size distribution of the EV sample was also preserved after
211 purification, indicating minimal loss of EVs (Figures 4c and d).

212

213 **2.5 Isolation and Purification of EGFR EVs from DiFi Cell Lines**

214 A major research direction in the EV field is to identify EVs secreted from specific (diseased) cells or by
215 specific pathways¹⁴. In this study, EVs were first isolated from human colorectal cancer cells (DiFi)
216 by ANM (asymmetrical nanoporous membrane). Then specific EVs with EGFR membrane proteins were
217 isolated by the MNM to accurately quantify the miRNA content of specific EVs. Based on analysis of
218 EGFR-containing DiFi EVs, isolated EVs were likely exosomes based on tetraspanin content³⁴. Some
219 of the EVs released by the DiFi cells exhibited inactive EGFR and active EGFR³⁴. We utilized a total
220 EGFR antibody that captures both active and inactive EGFR in this experiment. DiFi cell culture super-
221 natants were first processed by tangential flow filtration with 30nm asymmetric nanoporous mem-
222 branes³³ to remove free-floating proteins. Briefly, 1 μ g anti-EGFR antibodies were added into the sample
223 and incubated for 30min. After adding 100 μ L anti-rabbit IgG microBeads (30nm, Milyteni Biotech) and
224 incubating for 1 hr, the mixture was passed through the MNM. We extracted miRNA from all fractions
225 during the process and performed qRT-PCR to assess miR-21 levels. Figure 5b shows miRNA content
226 inside the isolated EGFR EVs, and the flow-through material add up equally to the total miR-21 levels
227 in the original sample with 21% error, which is insignificant considering qRT-PCR can only differentiate
228 2-fold changes. The total amount of EGFR in the ANM isolate and MNM flow through is also measured

229 by ELISA. A drop of close to 90% was achieved, indicating most of EGFR were captured in the MNM
230 EGFR isolate (Figure 5b inset). To further explore the quantification potential of our system, we did the
231 same experiment on both undiluted and 8× diluted ANM-processed DiFi samples. As shown in Figure
232 5c, the 8.3-fold change in miR-21 expression level matches the dilution factor, suggesting our high-
233 efficiency is consistent among different initial sample concentrations, which is important for quantitative
234 biomarker studies.

235

236 **3 Discussion**

237 Here, we demonstrated the utility and efficiency of electroplated MNM with unique heterogeneous su-
238 perparamagnetic junctions. This method can achieve high-efficiency capture of superparamagnetic nano-
239 beads. We achieved almost 100% nanobead recovery from the solution at up to 5mL/hr on a single de-
240 vice. The uncaptured EVs can go through the straight pores and be collected in the flow-through. We
241 proved our device's efficiency and specificity using HDL as a model, with >80% of HDL particles re-
242 covered and minimal non-specific retention at less than 15%. The high and consistent yield of our system
243 provides quantification potential for studies of EVs, lipoproteins, and other extracellular RNA carriers.
244 We further demonstrated the performance of MNM in exosome capture, purification of HDL-enriched
245 EV samples, and EGFR-positive EVs characterization. Our platform is also applicable for other molec-
246 ular or virus immunocapture applications where capture efficiency and throughput are essential.

247

248 **4 Methods**

249 **4.1 Numerical Simulations**

250 COMSOL was used to model and simulate different nanopore structures to estimate the magnetic flux
251 density and its gradient. A two-dimensional (2D) axial-symmetry geometry model was used with the
252 Magnetic Fields, No Currents interface in the AC/DC module. The software built-in NiFe B-H curve was
253 used. A static magnetic flux density of 0.5T was applied at the far boundary of the model. The simulation
254 was conducted with a physics-controlled meshing of extremely fine elements. More details have been
255 shown in the Supporting Information.

256

257 **4.2 Microscopy Imaging**

258 Surface SEM images were taken with Magellan 400. For EV-captured membranes, 2% EMS-quality
259 paraformaldehyde aqueous solution was used for fixation, and 2nm gold was sputtered in advance for
260 conductivity. Vesicles were examined under low beam energies. Cross-sections of the nanopores were
261 prepared using the Helios G4 UX DualBeam (Thermo Scientific). After protecting the cross-section sur-
262 face with Pt EBID, slices of 5nm thickness were sequentially obtained with Auto Slice & View™ 4
263 (AS&V4) software operating with a focused 10keV beam of gallium ions. The slicing was stopped at the
264 center of the pore and the images were acquired with a voltage of 3kV using a TLD detector for secondary
265 electrons.

266

267 **4.3 Ni₈₀Fe₂₀ Deposition by Electroplating**

268 To fabricate the electroplated magnetic nanoporous membrane, 80nm Au was deposited onto the tracked-
269 etched PET films in an FC-1800 Evaporator. The gold layer provides good adhesiveness between poly-
270 mer and NiFe and functions as a seed layer for electroplating. The membrane was cut into 4cm × 4cm
271 pieces. Copper tapes were used to fix membranes onto the support and electrically connected to cathode.
272 Nickel plate was used as the anode. The electroplating solution adopted from the literature^{35,36} can be
273 found in Table S1. Constant current density at 2mA/cm² was applied by Keithley 2636A Dual-Channel
274 System SourceMeter; voltage is monitored during the electroplating process. A custom electroplating
275 stirring tank was designed for uniform deposition. The deposition rate was derived by SEM images on
276 thicker samples grown under the same conditions. Another 10nm Au was deposited on the top of the
277 NiFe layer to reduce nonspecific adsorption and chemical instability.

278

279 **4.4 Ni₈₀Fe₂₀ Deposition by Sputtering**

280 Same as the electroplated samples, 80nm Au were deposited onto the PET films initially. The sputtered
281 samples were prepared at room temperature in a commercial UHV sputtering system Oerlikon DCSS
282 using a Ni₈₀Fe₂₀ target. Ar gas flow was fixed to 20sccm, and the plasma power was 50W during

283 deposition. The deposition rate was derived by means of stylus profilometer and SEM images on thicker
284 samples grown under the same conditions. After sputtering, 10nm Au was deposited at the top of the
285 NiFe layer.

286

287 **4.5 Plasma Samples**

288 De-identified plasma samples were obtained from Zen-Bio Inc. and consisted of 10mL of fresh human
289 plasma collected in tubes with EDTA coagulant. Each sample was tested for pathogens as required by
290 the FDA.

291

292 **4.6 DiFi Cell Culture Conditioned Media Collection**

293 DiFi cells were grown in a C2011 FiberCell bioreactor with 20kDa pore using manufacturer's instruc-
294 tions (FiberCell Systems, New Market, MD) using FiberCell systems' defined serum free media (CDM-
295 HD). Specifically, the bioreactor was washed overnight with sterile 1X DPBS (Corning, Corning, NY)
296 and then overnight with high glucose DMEM (hgDMEM/ Corning). The bioreactor was treated with
297 0.5mg of bovine fibronectin (Sigma, St. Louis, MO) in 20ml of DMEM for 4 hrs to overnight. The
298 bioreactor was then washed overnight with complete hgDMEM with 10% bovine growth serum, (1%
299 Penicillin-Streptomycin [Pen/Strep, GIBCO, Dublin/Ireland], 1% Glutamine [GIBCO], 1% glutamine
300 [GIBCO], 1% non-essential amino acids [GIBCO]). The bioreactor was loaded with $1-5 \times 10^8$ DiFi cells
301 in complete hgDMEM with 10% serum and allowed to stand for 1 hr before circulating complete DMEM
302 with 10% serum. Glucose levels were monitored daily with a glucometer (CESCO bioengineering, Tre-
303 vose, PA) and when glucose levels were at half of that in starting media, the media bottle was replaced.
304 In subsequent media changes the bioreactor went from 10% bovine serum, to 5% then to 3%, before
305 switching to 10% CDM-HD (DMEM-HD) media. Once cells are established in DMEM-HD (at least two
306 weeks in DMEM-HD) routine harvest of conditioned media was performed, removing 20ml of condi-
307 tioned media per day. Collected media was spun at 2000 RPMs to remove cells and any large debris,
308 then a subfraction of the media was additionally gravity filtered through a Millex 0.22um pore syringe
309 filter (Millipore Sigma, Burlington, MA). At least 3 days of filtered media collections were pooled.

310

311 **4.7 Lipoprotein Collection**

312 Plasma was collected from consented human participants under active Vanderbilt IRB protocols and
313 guidance. Blood was drawn into EDTA-containing collection tubes and immediately centrifuged to sep-
314 arate plasma. HDL and LDL were isolated from human plasma by KBr density-gradient ultracentrifuga-
315 tion (DGUC), as previously described³². Briefly, native LDL (1.019-1.062g/L) and HDL (1.063-
316 1.021g/L) were isolated by sequential DGUC using an Optima XPN-80 Ultracentrifuge with SW41Ti or
317 SW32Ti rotors (Beckman-Coulter). HDL and LDL were dialyzed in PBS with >4 buffer changes, and
318 concentrated with 3,000 Da m.w. cutoff filters (Millipore). Total protein levels were determined for each
319 lipoprotein sample (HDL and LDL) by BCA colorimetric assays (Pierce, ThermoFisher).

320

321 **4.8 Cholesterol Assay**

322 Cholesterol Quantification Assay Kit (Sigma-Aldrich, CS0005) was used to measure the cholesterol con-
323 centration of samples. Briefly, 44 μ L Assay Buffer, 2 μ L Probe, 2 μ L Enzyme Mix, 2 μ L Cholesterol Es-
324 terase, and 50 μ L sample were mixed and incubated at 37°C for 30min in each well. Calibration curve
325 was established for every measurement with standard samples with 0-5 μ g cholesterol. All samples were
326 diluted to the range of calibration curve with the Assay Buffer. Absorbance at 570nm was measured and
327 compared to the standards on the same plate to determine total cholesterol.

328

329 **4.9 qRT-PCR**

330 miRNAs were isolated from samples using the NucleoSpin® miRNA Plasma Kit (Takara Bio) according
331 to the manufacturer's manual. 300 μ L of the sample was first mixed with 90 μ L MLP solution and incu-
332 bated at room temperature for 3min, followed by adding 30 μ L MPP buffer and 1min room temperature
333 incubation. 3.5 μ L (1.6 \times 10⁸ copies/ μ L) of cel-miR-39-3p in RNase-free water was added into the lysate
334 as a normalization spiked-in control. Then the mixture was centrifuged at 11000 \times g. The supernatant was
335 taken and mixed with 400 μ L isopropanol. The mixture was transferred into the binding column and
336 centrifuged at 11000 \times g for 30s. The column was then washed with 100 μ L MW1 and 700 μ L MW2 se-
337 quentially at 11000 \times g for 30s, followed by 250 μ L MW2 washing and drying at 11000 \times g for 3min. Fi-
338 nally, 30 μ L RNase-free water was added to elute the miRNA at 11000 \times g for 1min after incubation at

339 room temperature for 1min. Reverse transcription was carried out using a miScript II RT Kit (Qiagen). A
340 20 µL reverse transcription reaction was prepared with 2.2 µL of eluted miRNA, 4 µL 5· miScript HiSpec
341 Buffer (Qiagen), 2 µL 10· miScript Nucleics Mix (Qiagen), 9.8 µL RNase-free water, and 2 µL miScript
342 Reverse Transcriptase Mix (Qiagen). The reaction was incubated at 16°C for 60 min followed by 95°C
343 for 5 min. The reverse transcription reaction was then diluted with 200 µL RNase-free water. Triplicates
344 of qPCR reactions were carried out using miScript SYBR Green PCR Kit (Qiagen) and run on a
345 StepOnePlus™ Real-Time PCR System (Applied Biosystems). The reaction contained 2 µL diluted
346 cDNA, 12.5 µL 2· QuantiTect® SYBR Green PCR Master Mix (Qiagen), 2.5 µL 10· miScript Universal
347 Primer (Qiagen), 10· miScript Primer Assay (Qiagen) for the target miRNA, and 5.5 µL RNase-free water
348 in a final volume of 25 µL. The reaction mixtures were incubated for 15 min at 95°C, followed by 45
349 cycles of 94°C for 15 s, 55°C for 30 s, and 70°C for 30 s. The C_q values were acquired and analyzed
350 using StepOne™ Software v2.3 in accordance with the MIQE guidelines (Bustin et al., 2013). The C_q
351 values of the target miRNAs were adjusted by spiked-in standard control (cel-miR-39-3p) added during
352 miRNA extraction.

353

354 **4.10 ELISA**

355 A human EGFR ELISA kit (EGFR0, R&D Systems™) was used to quantify the EGFR in the samples.
356 100 µL of Assay Diluent and 50 µL of standard, control, or sample were added to each well in the mi-
357 croplate, followed by 2 hrs incubation at room temperature. After 4 times of aspirating and washing each
358 well, 200 µL of Human EGFR Conjugate was added to each well and incubated for 2 hrs at room tem-
359 perature, followed by 4 washes. 200 µL of Substrate Solution was added to each well and incubated for
360 30 minutes at room temperature, and then 50 µL of Stop Solution was added to each well. Absorbance
361 at 450nm subtracted by readings at 540nm was measured. The EGFR concentration was determined by
362 the readings and the established calibration curve.

363

364 **4.11 Nanoparticle Tracking Analysis**

365 Nanoparticle tracking analysis (NTA) was performed using a NanoSight NS300 (NanoSight Ltd., Ames-
366 bury, UK). All samples were diluted to the optimal working particle range prior to measurements using

367 1×PBS. Five 60s videos were recorded of each sample with camera level set at 10. A constant flow rate
368 setting of 1000 was maintained during the recording. The temperature was monitored throughout the
369 measurements. The instrument was flushed with 1×PBS between measurements. Videos recorded for
370 each sample were analyzed with NTA software to determine the concentration and size distribution of
371 measured particles with corresponding standard error. The same detection threshold was used for analy-
372 sis.

373 **5 Conflicts of interest**

374 There are no conflicts to declare.
375

376 **6 Data availability**

377 The data that support the findings of this study are available within the article and Supplementary Infor-
378 mation files, or available from the corresponding authors on request. Source data are provided with this
379 paper.

380 **7 Acknowledgments**

381 The authors acknowledge the support of NIH Common Fund, through the Office of Strategic Coordina-
382 tion/Office of the NIH Director, 1UH3CA241684-01. C.Z. acknowledge the support of a China Schol-
383 arship Council fellowship. R.J.C. acknowledges support of NCI R35 CA197570. The authors
384 acknowledge the support of the Cancer Cure Venture (CCV) Grant, made possible by Walther Cancer
385 Foundation.
386

387 **8 Author Contributions**

388 C.Z. and X.H. contributed equally to this work. C.Z., X.H., C.W., and H.C.C. conceived the idea and
389 designed the study. C.Z. performed the finite element simulations. C.Z., X.H., and C.W. performed the
390 experiments. C.Z. analyzed the results and wrote the manuscript with inputs from all authors. Y.Z., L.X.,

391 J.N.H., J.L.F, K.C.V., and R.J.C. provided biological samples. C.W., S.S., and H.C.C. supervised the
392 project.

393

394 **References**

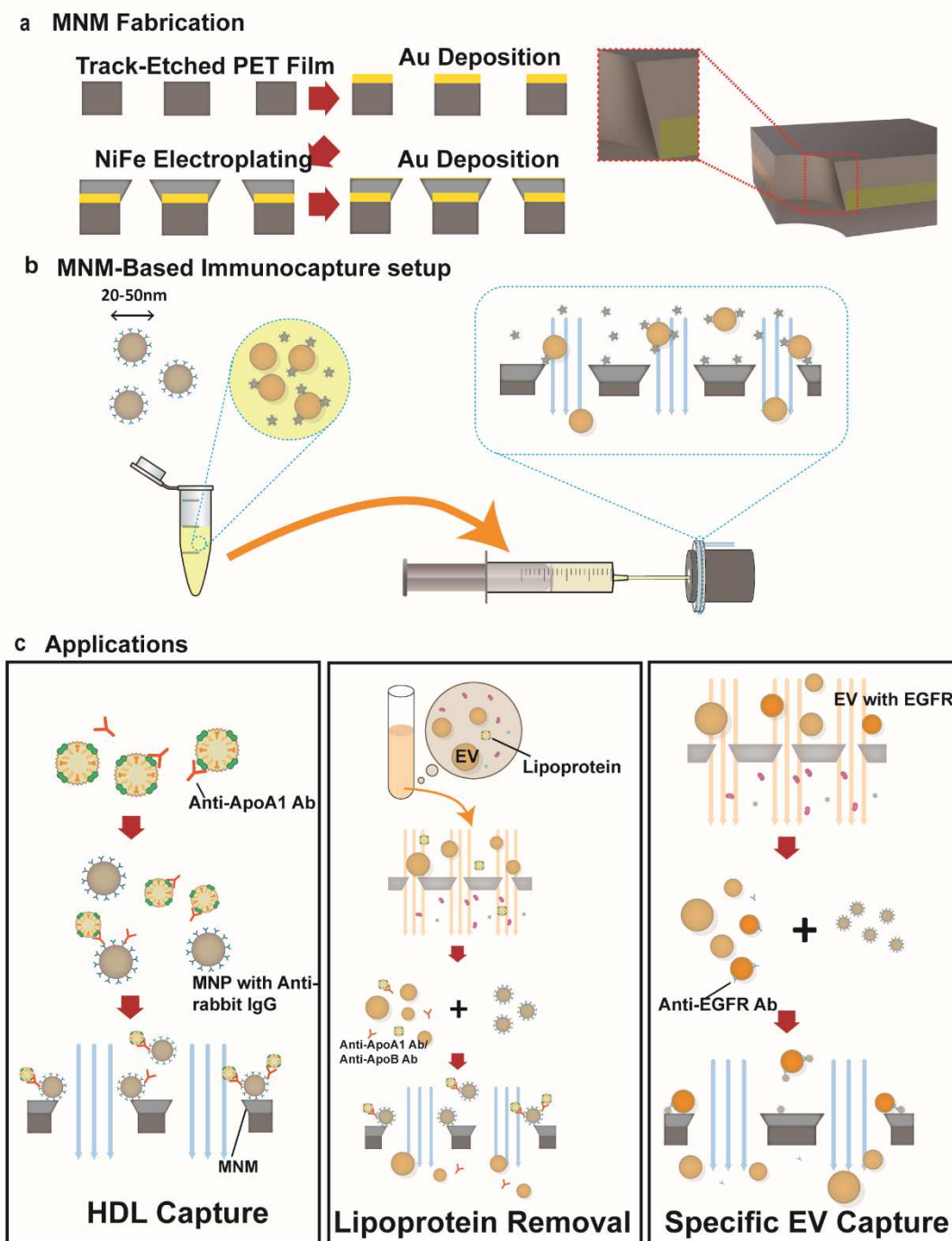
- 395 1. Valadi, H. *et al.* Exosome-mediated transfer of mRNAs and microRNAs is a novel mechanism of
396 genetic exchange between cells. *Nat. Cell Biol.* **9**, 654–659 (2007).
- 397 2. Mathivanan, S., Ji, H. & Simpson, R. J. Exosomes: extracellular organelles important in intercellular
398 communication. *J. Proteomics* **73**, 1907–1920 (2010).
- 399 3. Simonsen, J. B. What Are We Looking At? Extracellular Vesicles, Lipoproteins, or Both? *Circ. Res.*
400 **121**, 920–922 (2017).
- 401 4. Vlassov, A. V., Magdaleno, S., Setterquist, R. & Conrad, R. Exosomes: current knowledge of their
402 composition, biological functions, and diagnostic and therapeutic potentials. *Biochim. Biophys. Acta*
403 **1820**, 940–948 (2012).
- 404 5. Jeppesen, D. K. *et al.* Reassessment of Exosome Composition. *Cell* **177**, 428–445.e18 (2019).
- 405 6. Zhuang, G. *et al.* Tumour-secreted miR-9 promotes endothelial cell migration and angiogenesis by
406 activating the JAK-STAT pathway. *EMBO J.* **31**, 3513–3523 (2012).
- 407 7. Hunter, M. P. *et al.* Detection of microRNA Expression in Human Peripheral Blood Microvesicles.
408 *PLoS ONE* **3**, (2008).
- 409 8. Minciacchi, V. R., Freeman, M. R. & Di Vizio, D. Extracellular Vesicles in Cancer: Exosomes,
410 Microvesicles and the Emerging Role of Large Oncosomes. *Semin. Cell Dev. Biol.* **40**, 41–51
411 (2015).
- 412 9. Fujita, Y., Yoshioka, Y. & Ochiya, T. Extracellular vesicle transfer of cancer pathogenic compo-
413 nents. *Cancer Sci.* **107**, 385–390 (2016).
- 414 10. Kosaka, N., Yoshioka, Y., Fujita, Y. & Ochiya, T. Versatile roles of extracellular vesicles in cancer.
415 *J. Clin. Invest.* **126**, 1163–1172 (2016).
- 416 11. Cromwell, W. C. & Otvos, J. D. Heterogeneity of low-density lipoprotein particle number in patients
417 with type 2 diabetes mellitus and low-density lipoprotein cholesterol <100 mg/dl. *Am. J. Cardiol.*
418 **98**, 1599–1602 (2006).

- 419 12. Crescitelli, R. *et al.* Distinct RNA profiles in subpopulations of extracellular vesicles: apoptotic
420 bodies, microvesicles and exosomes. *J. Extracell. Vesicles* **2**, 20677 (2013).
- 421 13. Akinkuolie, A. O., Paynter, N. P., Padmanabhan, L. & Mora, S. High-density lipoprotein particle
422 subclass heterogeneity and incident coronary heart disease. *Circ. Cardiovasc. Qual. Outcomes* **7**,
423 55–63 (2014).
- 424 14. Coumans, F. A. W. *et al.* Methodological Guidelines to Study Extracellular Vesicles. *Circ. Res.* **120**,
425 1632–1648 (2017).
- 426 15. Willms, E., Cabañas, C., Mäger, I., Wood, M. J. A. & Vader, P. Extracellular Vesicle Heterogeneity:
427 Subpopulations, Isolation Techniques, and Diverse Functions in Cancer Progression. *Front. Immu-*
428 *nol.* **9**, (2018).
- 429 16. Wu, Y., Deng, W. & Klinke, D. J. Exosomes: Improved methods to characterize their morphology,
430 RNA content, and surface protein biomarkers. *The Analyst* **140**, 6631–6642 (2015).
- 431 17. Jeyaram, A. & Jay, S. M. Preservation and Storage Stability of Extracellular Vesicles for Therapeu-
432 tic Applications. *AAPS J.* **20**, 1 (2017).
- 433 18. Clayton, A. *et al.* Analysis of antigen presenting cell derived exosomes, based on immuno-magnetic
434 isolation and flow cytometry. *J. Immunol. Methods* **247**, 163–174 (2001).
- 435 19. Mathivanan, S. *et al.* Proteomics analysis of A33 immunoaffinity-purified exosomes released from
436 the human colon tumor cell line LIM1215 reveals a tissue-specific protein signature. *Mol. Cell.*
437 *Proteomics MCP* **9**, 197–208 (2010).
- 438 20. Koga, K. *et al.* Purification, characterization and biological significance of tumor-derived exosomes.
439 *Anticancer Res.* **25**, 3703–3707 (2005).
- 440 21. Issadore, D., YELLESWARAPU, V. & KO, J. Magnetic separation filters and microfluidic devices
441 using magnetic separation filters. (2017).
- 442 22. Ko, J. *et al.* Combining Machine Learning and Nanofluidic Technology To Diagnose Pancreatic
443 Cancer Using Exosomes. *ACS Nano* **11**, 11182–11193 (2017).
- 444 23. Thamida, S. K. & Chang, H.-C. Nonlinear electrokinetic ejection and entrainment due to polariza-
445 tion at nearly insulated wedges. *Phys. Fluids* **14**, 4315–4328 (2002).
- 446 24. Wang, C., Sensale, S., Pan, Z., Senapati, S. & Chang, H.-C. Slowing down DNA translocation
447 through solid-state nanopores by edge-field leakage. *Nat. Commun.* **12**, 140 (2021).

- 448 25. Barbry, M. *et al.* Atomistic Near-Field Nanoplasmonics: Reaching Atomic-Scale Resolution in Na-
449 noptics. *Nano Lett.* **15**, 3410–3419 (2015).
- 450 26. Imura, K., Nagahara, T. & Okamoto, H. Near-Field Two-Photon-Induced Photoluminescence from
451 Single Gold Nanorods and Imaging of Plasmon Modes. *J. Phys. Chem. B* **109**, 13214–13220 (2005).
- 452 27. Wang, Y., Plouraboue, F. & Chang, H.-C. Broadband converging plasmon resonance at a conical
453 nanotip. *Opt. Express* **21**, 6609–6617 (2013).
- 454 28. El-makadema, A., Rashid, L. & Brown, A. K. Geometry Design Optimization of Large-Scale Broad-
455 band Antenna Array Systems. *IEEE Trans. Antennas Propag.* **62**, 1673–1680 (2014).
- 456 29. Eteng, A. A., Abdul Rahim, S. K. & Leow, C. Y. Geometrical Enhancement of Planar Loop Anten-
457 nas for Inductive Near-Field Data Links. *IEEE Antennas Wirel. Propag. Lett.* **14**, 1762–1765 (2015).
- 458 30. Wang, Y., Chang, T. C. & Stoddart, P. R. Diffraction-limited ultrasensitive molecular nano-arrays
459 with singular nano-cone scattering. *Biomicrofluidics* **8**, 10–14 (2014).
- 460 31. Pegg, L.-J. & Hatton, R. A. Nanoscale Geometric Electric Field Enhancement in Organic Photovol-
461 taics. *ACS Nano* **6**, 4722–4730 (2012).
- 462 32. Michell, D. L. *et al.* Isolation of High-density Lipoproteins for Non-coding Small RNA Quantifica-
463 tion. *J. Vis. Exp. JoVE* (2016) doi:10.3791/54488.
- 464 33. Wang, C., Senapati, S. & Chang, H.-C. Liquid biopsy technologies based on membrane microfluid-
465 ics: High-yield purification and selective quantification of biomarkers in nanocarriers.
466 *ELECTROPHORESIS* **41**, 1878–1892 (2020).
- 467 34. Zhang, Q. *et al.* Supermeres are functional extracellular nanoparticles replete with disease bi-
468 omarkers and therapeutic targets. *Nat. Cell Biol.* **23**, 1240–1254 (2021).
- 469 35. Smistrup, K., Tang, P. T. & Moller, P. Pulse Reversal PermAlloy Plating Process for MEMS Ap-
470 plications. *ECS Trans.* **3**, 179–189 (2007).
- 471 36. Schiavone, G. *et al.* Integration of Electrodeposited Ni-Fe in MEMS with Low-Temperature Depo-
472 sition and Etch Processes. *Materials* **10**, (2017).

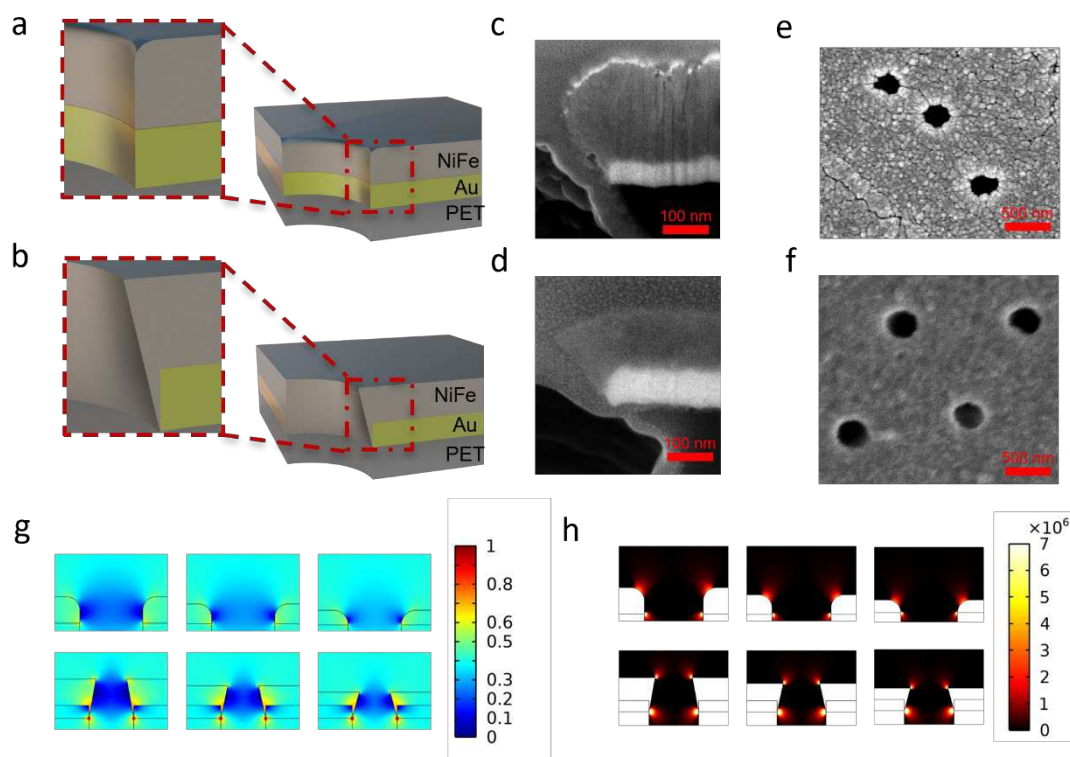
473

474



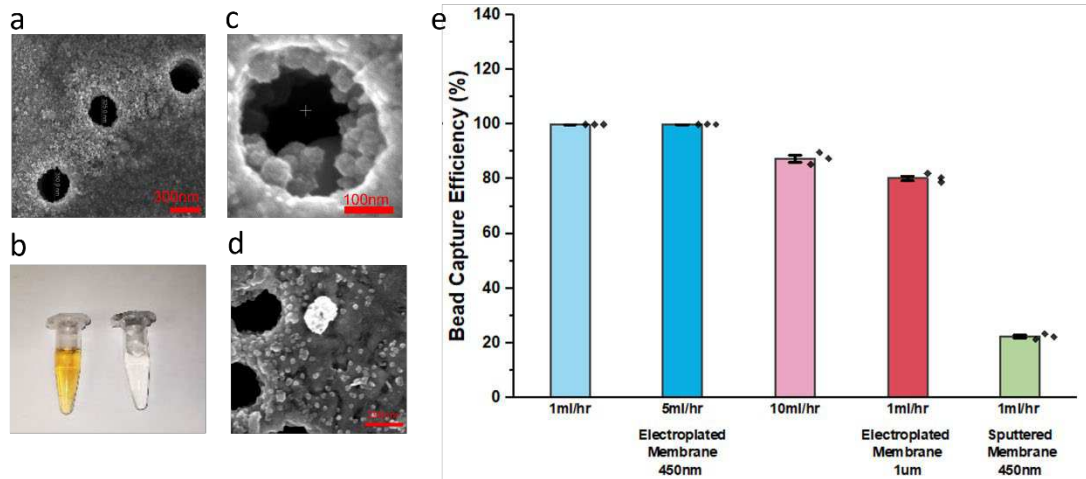
476 **Schematic 1.** Schematic of the experimental procedure. a) Fabrication of the magnetic nanoporous
 477 membrane (MNM). 80nm Au was deposited onto the tracked-etched PET film to provide good adhesion
 478 and electric conductivity for electroplating. Then 200nm NiFe film was deposited onto the mem-
 479 branewith electroplating. The heterogeneous nanowedge junction at the edge of the nanopore on the
 480 membrane is highlighted. b) MNM-based immunocapture setup. First the antibody and antigen were
 481 incubated to form Ab-Ag complex, followed by incubating with magnetic nanobeads which were conju-
 482 gated with anti-rabbit IgG antibodies. Then the diluted sample was run through the chamber of the MNM
 483 device with syringe and pump. The MNM device was assembled with the MNM sandwiched between
 484 two 3D-printed chips. The device was assembled between two magnets, with the magnet near the inlet

485 was in ring-shape. The magnetic beads were captured onto the edge of the nanopores as highlighted. c)
 486 Experimental steps of the three applications. Anti-ApoA1 antibodies were used to capture HDL; Asy-
 487 metric nanopore membrane was used to isolate the EVs, with small amount of HDL remained, and we
 488 use MNM to remove the residual HDL to purify the EV fraction; In the EV fraction, MNM was utilized
 489 to capture the specific EV with certain surface protein, i.e. EGFR.
 490



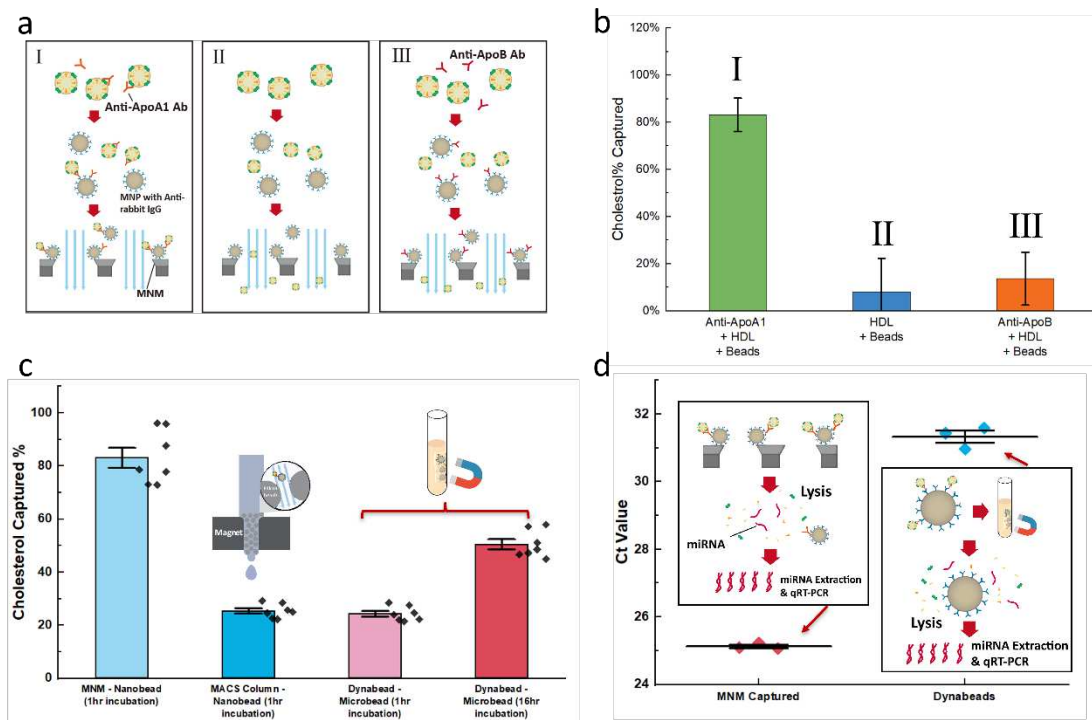
492 **Figure 1.** Characterization of the nanopores on the sputtered and electroplated MNM. Schematic of
 493 the nanopores on a) a sputtered magnetic nanoporous membrane and b) an electroplated magnetic na-
 494 nanoporous membrane, and the edge of the nanopore is highlighted. c) Cross-section SEM images of a
 495 single nanopore on a sputtered magnetic nanoporous membrane. Note the smooth edge of the NiFe layer.
 496 d) Cross-section SEM images of a single nanopore on an electroplated magnetic nanoporous membrane.
 497 Note the sharp edge of the NiFe layer. SEM images of the e) electroplated membrane and f) sputtered
 498 membrane. g) Simulation of magnetic flux density in nanopores on ideal sputtered magnetic nanoporous
 499 membrane (upper) and ideal electroplated magnetic nanoporous membranes (lower), showing the dra-
 500 matic amplification of the flux density at the wedge on the electroplated MNM (Membrane thickness left
 501 to right: 200nm, 150nm, 100nm). h) Simulation of magnetic field, showing the gradient of flux density
 502 norm square at the wedge on both ideal sputtered magnetic nanoporous membranes (upper) and ideal
 503 electroplated magnetic nanoporous membranes (lower) (Membrane thickness left to right: 200nm,
 504 150nm, 100nm).

505
 506



508 **Figure 2.** Characterization of the magnetic beads capture of MNM. a) SEM image of captured mag-
 509 netic beads near the edges of nanopores by the monopole field. The diameter of the pore has decreased
 510 to around 300nm after the deposition of different metallic layers. b) Zoomed-in SEM image shows nano-
 511 beads captured inside a single nanopore by the dipole field of the wedge junction. c) Solution of beads
 512 before passing through the magnetic nanoporous membrane (left) and after filtering through the magnet-
 513 ized membrane (right). The yellow color indicates the concentrated beads. d) SEM image of mouse
 514 plasma exosome captured near the nanopore. e) Bead capture efficiency of sputtered and electroplated
 515 membranes at different flow rates and pore size. For the electroplated membrane, original pore size of
 516 450nm and 1µm, and flow rate of 1mL/hr, 5mL/hr and 10mL/mL have been tested. For the sputtered
 517 membrane, original pore size of 450nm and flow rate of 1mL/hr have been tested.

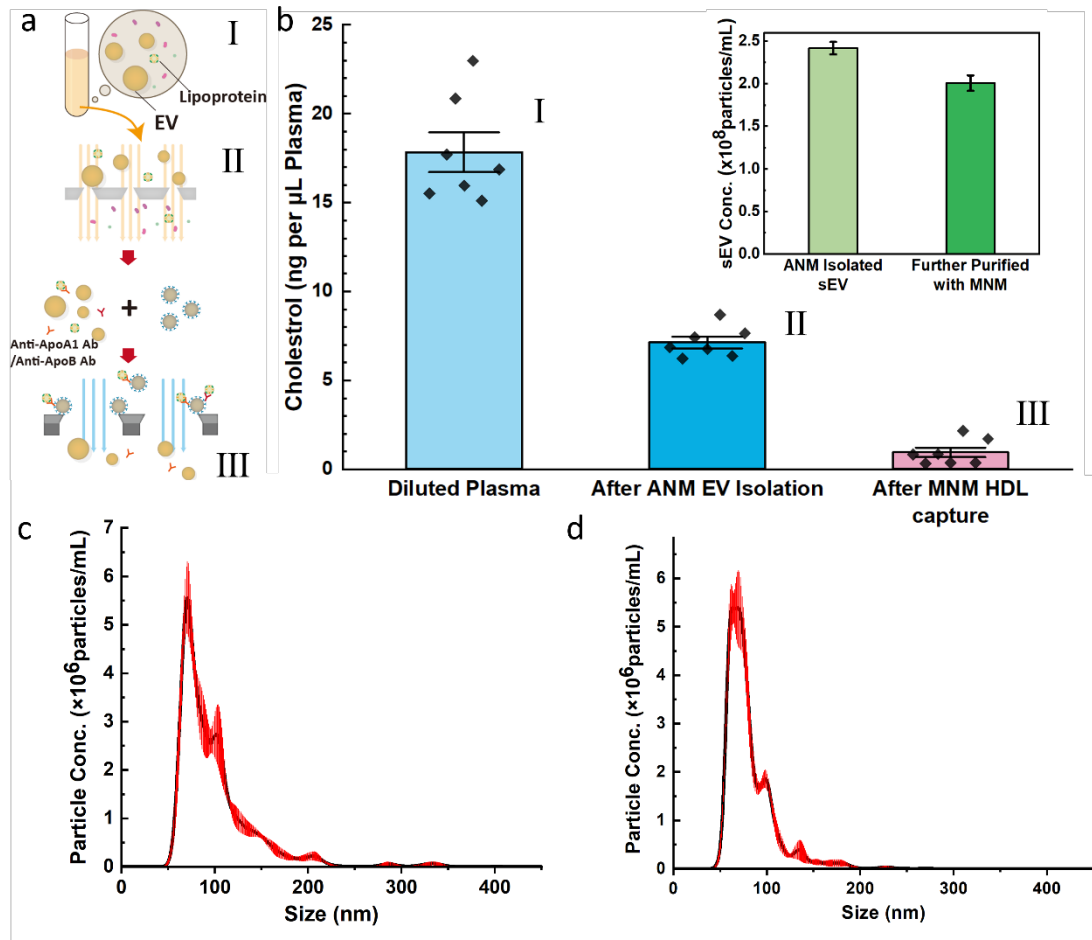
518
 519



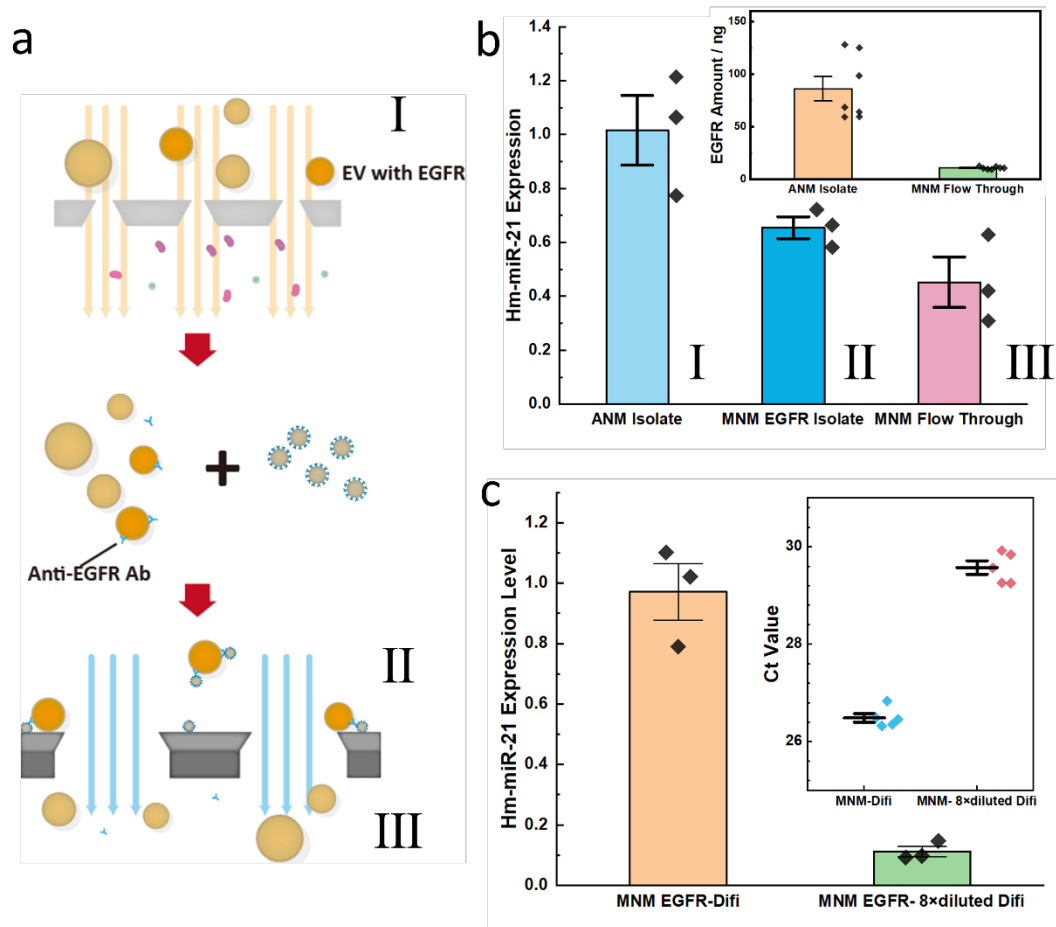
522 **Figure 3.** Characterization of the HDL capture rate. a) Schematic of the immunocapture of HDL capture
 523 rate using cholesterol as a measure. In the three cases, different combinations were tested for specific
 524 capture of HDL with anti-ApoA1 antibodies, and nonspecific capture with no antibodies and anti-ApoB
 525 antibodies which are specific to LDL. b) Capture rate of the three cases in a). c) Comparison of HDL
 526 capture rate using different immunocapture kits, including the Miltenyi MACS™ μ Column and Ther-
 527 mofisher Dynabeads™. The inset schematics show the basic working principle of different technologies.
 528 The incubation time was chosen to be 1h and 16h for Dynabeads™. d) Ct value of miR-21 from qRT-
 529 PCR experiments. MiRNA samples were extracted from HDL captured by both MNM and Dynabeads™
 530 with the same starting sample volume. The incubation time of the MNM experiment is 1h and that of
 531 Dynabeads™ is 12h. The schematics of the immunocapture and qRT-PCR were shown in the inset. The
 532 HDL was captured by MNM or Dynabeads and then lysed, followed by miRNA extraction and qRT-
 533 PCR.

534

535



537 **Figure 4.** Characterization of the HDL removal from the fractionated EV. a) Schematic of the EV
 538 fractionation and immunocapture of HDL. The diluted plasma (sample I) run through the asymmetric na-
 539 nanoporous membrane to remove other particles with size exclusion mechanism, thus obtaining the EV
 540 fraction (sample II). Due to the dominating amount of HDL, a small portion of HDL was remained in the
 541 EV fraction, so it was incubated with anti-ApoA1 and anti-ApoB antibodies and then magnetic nano-
 542 beads conjugated with anti-rabbit IgG antibodies, and run through the MNM device to remove the HDL,
 543 and the flowthrough was collected (sample III). b) Lipoproteins (cholesterol) remnant at different stages
 544 of purification from samples I, II, III in a), and (inset) EV concentration before and after MNM im-
 545 munocapture (sample II and III). Size distribution of EV samples with NTA c) before (sample II) and d)
 546 after MNM immunocapture (sample III).
 547



549 **Figure 5.** Characterization of the immunocapture of specific EV, i.e. EV with EGFR. a) Schematic of
 550 the EV fractionation and immunocapture of EV with EGFR. The Difi cell culture medium was run
 551 through the asymmetric nanoporous membrane to obtain the EV fraction (sample I), which was then incu-
 552 cated with the anti-EGFR antibodies and then magnetic nanobeads conjugated with anti-human IgG an-
 553 tibodies. Then the samples passed through the MNM device, with the captured sample on the mag-
 554 netic membrane mixed with lysing buffer (sample II), and the flowthrough was collected (sample III). b)
 555 Hm-miR-21 expression level of different DiFi exosomes fractions from samples I, II, III in a). The total
 556 amount of EGFR was also measured for I and III. c) Expression level of Hm-miR-21 in the EGFR exo-
 557 somes before and after 8× dilution of the DiFi samples, and the Ct value of their qRT-PCR results.

558
 559

Supplementary Files

This is a list of supplementary files associated with this preprint. Click to download.

- [MNMNCSubmissionSI.pdf](#)